

G²SF-MIAD: Geometry-Guided Score Fusion for Multimodal Industrial Anomaly Detection

Chengyu Tao, XuanmingCao, and Juan Du *Senior Member, IEEE*

Abstract—Industrial quality inspection plays a critical role in modern manufacturing by identifying defective products during production. While single-modality approaches using either 3D point clouds or 2D RGB images suffer from information incompleteness, multimodal anomaly detection offers promise through the complementary fusion of crossmodal data. However, existing methods face challenges in effectively integrating unimodal results and improving discriminative power. To address these limitations, we first reinterpret memory bank-based anomaly scores in single modalities as isotropic Euclidean distances in local feature spaces. Dynamically evolving from Euclidean metrics, we propose a novel **Geometry-Guided Score Fusion (G²SF)** framework that progressively learns an anisotropic local distance metric as a unified score for the fusion task. Through a geometric encoding operator, a novel **Local Scale Prediction Network (LSPN)** is proposed to predict direction-aware scaling factors that characterize first-order local feature distributions, thereby enhancing discrimination between normal and anomalous patterns. Additionally, we develop specialized loss functions and score aggregation strategy from geometric priors to ensure both metric generalization and efficacy. Comprehensive evaluations on the MVTEC-3D AD dataset demonstrate the state-of-the-art detection performance of our method with low positive rate and better recall, which is essential in industrial application, and detailed ablation analysis validates each component’s contribution. *(Code will be released upon acceptance).*

I. INTRODUCTION

Surface quality inspection is crucial in modern industries, as defects like scratches, dents, or cracks can severely impact product functionality and longevity, requiring automated and intelligent inspection systems for large-scale production. Since defective products are always rare in real-world scenarios, it has led to growing interest in unsupervised anomaly detection [1], [2], which uses only nominal (anomaly-free) samples for training, offering a practical solution for a wide range of industrial applications.

In complex industrial scenarios, unimodal anomaly detection methods often fail to comprehensively characterize defects due to the limitations of single data sources [3]. For instance, while 3D point clouds provide rich geometric details,

C. Tao is affiliated with the Academy of Interdisciplinary Studies, The Hong Kong University of Science and Technology, Hong Kong SAR, China (e-mail: ctaoaa@connect.ust.hk).

X.Cao is affiliated with the Smart Manufacturing Thrust, The Hong Kong University of Science and Technology (Guangzhou), Guangzhou, China (xcao743@connect.hkust-gz.edu.cn)

J. Du is affiliated with the Smart Manufacturing Thrust and the Data Science and Analytics Thrust at The Hong Kong University of Science and Technology (Guangzhou), Guangzhou, China; the Academy of Interdisciplinary Studies at The Hong Kong University of Science and Technology, Hong Kong SAR, China; and the Guangzhou HKUST Fok Ying Tung Research Institute, Guangzhou, China. (e-mail: juandu@ust.hk).

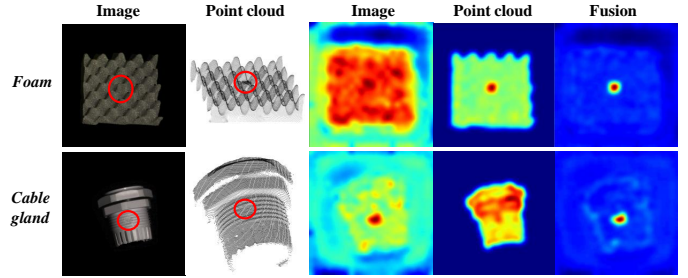


Fig. 1. Two representative examples from the MVTEC-3D AD dataset [2], including the original RGB image, 3D point cloud, and anomaly score maps from single modalities (image and point cloud) and multimodal fusion (the proposed G²SF). **Top**: Foam with a ‘cut’ anomaly, which is nearly invisible in the RGB image due to its complex texture. **Bottom**: Cable gland with a ‘thread’ anomaly, which is insufficiently discriminative in the point cloud as it only slightly alters the surface geometry.

they lack texture and color information in RGB images. By integrating these complementary modalities, multimodal approaches achieve superior performance. Fig. 1 illustrates two representative extreme scenarios from the MVTEC-3D AD dataset [2], where anomalies are predominantly undetectable in one specific modality.

Feature-based anomaly detection approaches have gained popularity due to their flexibility and strong performance [3]–[7]. These methods model the distributions of extracted features, obtained by either handcrafted descriptors or frozen networks, and assign feature-wise anomaly scores. For example, the memory bank-based methods, e.g., PatchCore [5], construct a memory bank of representative prototypes from the whole training dataset and define the anomaly score as the distance to the nearest prototype in the memory bank.

In multimodal scenarios, a challenge centers on developing effective fusion strategies to integrate detection results from individual modalities. Despite efforts to cross-modal relationships, existing methods typically employ simplistic strategies such as direct addition [3] or maximum value selection [8] of anomaly scores across modalities, while [7] utilizes a One-Class Support Vector Machine (OCSVM) for score combination. However, these methodologies face a critical limitation: unimodal anomaly scores frequently demonstrate insufficient discriminative capacity in practical applications. As visualized by Fig. 1, even normal regions in both point cloud and image data exhibit unexpectedly elevated anomaly scores. These unreliable unimodal assessments consequently compromise the fusion performance. To obtain more discriminative anomaly scores, feature adaptation [6], [9] can be applied

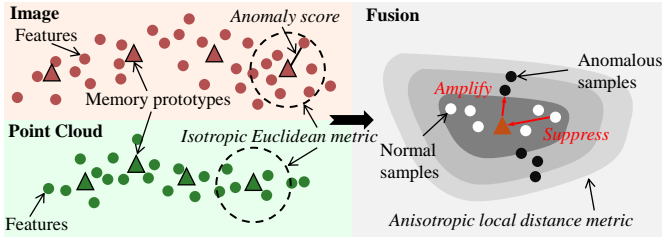


Fig. 2. **Left:** The anomaly score in memory bank-based methods, which is defined by the isotropic Euclidean distance to the nearest memory prototype. **Right:** The anisotropic local distance metric learned by G^2SF , suppressing anomaly scores for normal samples while amplifying the discrepancy for anomalies.

that adapts original features into more compact representations beforehand, followed by standard methods, e.g., PatchCore [5], to calculate final anomaly scores. One limitation is that critical details of original features essential for anomaly detection may be over-confidently compromised during first-step adaptation.

This paper re-examines memory bank-based unimodal approaches, revealing a fundamental geometric limitation for their insufficient discriminative capacity: Existing methods compute anomaly scores via isotropic Euclidean distances in local feature spaces centered on memory prototypes, as illustrated in Fig. 2, but critically ignore other local geometric characteristics (e.g., directional patterns) essential for anomaly detection. To address this limitation, we propose Geometry-Guided Score Fusion (G^2SF) - a framework that replaces isotropic distances with a learned anisotropic local distance metric for multimodal anomaly detection. Specifically, we introduce a Local Scale Prediction Network (LSPN) that derives direction-aware scaling factors to characterize local directional distributions of both modalities in the joint feature space. Subsequently, we formulate a fused metric combining these scales with original Euclidean distances from two modalities to amplify normal/anomaly discrepancies, as shown in Fig. 2.

Despite the enhanced discriminative power, our G^2SF offers two other advantages: (i) Instead of learning a new metric or anomaly detector from scratch, which are often risky in high-dimensional feature spaces [10], [11], perhaps increasing with multiple modalities involved, G^2SF explicitly quantifies how unimodal anomaly scores and local geometric structures in feature spaces contribute to the final metric. Consequently, it enables a progressive evolution from the Euclidean metric to an anisotropic metric, mitigating overfitting and ensuring robust metric learning (see Section III-D). (ii) As a one-stage anomaly detector, G^2SF maintains complete modality-specific information throughout the detection process (details are discussed in Section III-C), in contrast to existing feature adaptation frameworks [6], [9] aforementioned above.

The contributions of this paper are summarized as follows:

- We propose a systematic G^2SF framework for industrial multimodal anomaly detection by learning a unified discriminative metric in high-dimensional feature space.
- We propose a novel metric deformation paradigm, evolving from isotropic Euclidean metric to an anisotropic one. Specifically, throughout geometric encoding, we design

a new LSPN to predict direction-aware scaling factors, subsequently formulating the final metric.

- We propose critical loss functions to maintain specific geometric properties (e.g., metric consistency and cross-modal correspondence) during metric learning and a novel geometry-informed anomaly scoring strategy, enabling precise multimodal anomaly detection.
- Our method achieves the best performance on the MVTEC 3D-AD dataset, with particularly notable superiority at the AUPRO@1% metric, which corresponds to a very low false positive rate and better recall. This is highly valuable in real industrial applications.

II. LITERATURE REVIEW

A. 2D Image Anomaly Detection

Unsupervised anomaly detection methodologies can be broadly categorized into two paradigms: *reconstruction*-based approaches and *feature*-based techniques. Reconstruction-based methods typically employ generative architectures, e.g., transformers [12] and diffusion models [13], to establish pixel-level reconstruction fidelity for normal images. During the inference phase, anomaly detection is performed by calculating per-pixel discrepancies between input images and their reconstructed counterparts.

Feature-based approaches, in contrast, circumvent pixel-level comparisons by operating on informative handcraft or deep features. The central challenge in this paradigm involves effectively modeling the distribution of normal features. Existing solutions adopt different modeling strategies: PaDiM [14] represents features as multivariate Gaussian distributions across spatial positions, while CFlow-AD [15] employs conditional normalizing flows to capture more complex probability distributions. PNI [16] further enhances modeling by incorporating positional and neighborhood relationships of features. A notable method is PatchCore [5], which constructs a memory bank of representative normal features through coreset sampling. Owing to its robustness and adaptability, PatchCore has become a foundational method applicable to both 3D [3], multimodal [3], [6], [7], and noisy scenarios [17].

B. Multimodal 2D/3D Anomaly Detection

The pioneering MVTEC-3D AD dataset [2] benchmarks this task with various generative networks. For real-time requirement, Easy-Net [8] designs a multi-scale multimodal auto-encoder. Feature-based approaches also dominate in this field. CFM [18] constructs explicit one-to-one feature mappings to model the cross-modal relationship. For score fusion from different modalities, BTF [3] concatenates 2D/3D features with PatchCore [5], equivalent to linear score fusion. Based on the signed distance function (SDF) for 3D patch representation, Shape-Guided [19] establishes SDF-guided memory banks for fine-grained detection on image modality but relies on simplistic maximum value between image and SDF scores. M3DM [7] learns fused features by considering cross-modal interactions yet employs one-class SVM for data-driven score fusion of the original and fused features. However, the inherent limitations in the discriminative power of unimodal anomaly

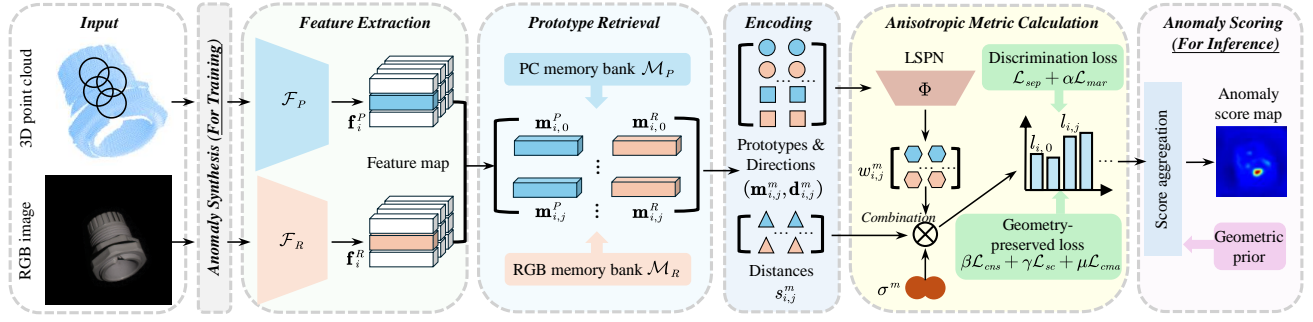


Fig. 3. Overall pipeline of the proposed G^2SF . During training, our model takes a pair of 3D point clouds and RGB images as inputs. The anomaly synthesis module (Section III-G) then injects synthetic anomalies into both modalities. Next, the nearest memory prototypes $\{\mathbf{m}_{i,j}^P, \mathbf{m}_{i,j}^R\}$ are retrieved from the 3D/2D memory banks $\mathcal{M}_P/\mathcal{M}_R$ (Section III-B). In Section III-C, the features $\mathbf{f}_i^P/\mathbf{f}_i^R$ are transformed into geometrically meaningful encodings, represented as triplets: $\langle \text{prototypes } \mathbf{m}_{i,j}^m, \text{directions } \mathbf{d}_{i,j}^m, \text{distances } s_{i,j}^m \rangle$ ($m \in \{P, R\}$). The LSPN Φ learns direction-aware scaling factors $w_{i,j}^m$ from $(\mathbf{m}_{i,j}^P, \mathbf{d}_{i,j}^P, \mathbf{m}_{i,j}^R, \mathbf{d}_{i,j}^R)$, which are combined with the distances $s_{i,j}^m$ and global scaling factors σ^m to compute the anisotropic local distance metric values $\{l_{i,j}^m\}$, as detailed in Section III-D. The learning process is supervised by two loss functions: the discrimination loss ($\mathcal{L}_{sep} + \alpha\mathcal{L}_{mar}$, Section III-E1) and the geometry-preserved loss ($\beta\mathcal{L}_{cns} + \gamma\mathcal{L}_{sc} + \mu\mathcal{L}_{cma}$, Section III-E2). Finally, during inference, a score aggregation strategy is applied, leveraging geometric priors for anomaly scoring, as described in Section III-F.

scores remain unaddressed. Toward this deficiency, LSFA [6] proposes a cross-modal feature adaptation paradigm that learns task-oriented features but risks overlooking the critical details of original features through adaptation.

Our G^2SF introduces two core advances over these existing approaches: (i) We learn a unified discriminative metric, eliminating suboptimal aggregation from unreliable unimodal anomaly scores; (ii) We introduce a dynamic metric deformation paradigm through isotropic-to-anisotropic evolution, preserving original modality-specific details while enabling precise discrimination in high-dimensional space.

III. METHODOLOGY

Our G^2SF aims to learn a unified anisotropic local distance metric for multimodal anomaly detection. The overall pipeline is illustrated in Fig. 3.

A. Feature Extraction

Our framework accepts a pair of 3D point cloud and RGB image as input. Specifically, we employ two frozen neural networks (\mathcal{F}_P and \mathcal{F}_R) to extract corresponding features \mathbf{f}_i^P (point cloud) and \mathbf{f}_i^R (image) at location i . Following existing methods [6], [7], [18], we adopt two vision transformers, DINO [20] for images and Point-MAE [21] for point clouds, considering their powerful representational capacity. \mathbf{f}_i^P and \mathbf{f}_i^R have high dimensions, i.e., 1152 and 768, respectively.

B. Prototype Retrieval from Memory Bank

Our G^2SF builds on the memory bank-based methods for unimodal anomaly detection. For each modality $m \in P, R$, we construct a memory bank \mathcal{M}^m that collects prototypical features from the entire training dataset following PatchCore [5]. Subsequently, for a feature \mathbf{f}_i^m , we can retrieve its $2k+1$ nearest neighbors $\{\mathbf{m}_{i,j}^m\}_{j=0}^{2k}$ from \mathcal{M}^m . Critically, the Euclidean distance between \mathbf{f}_i^m and the nearest $\mathbf{m}_{i,0}^m$ is typically defined as the anomaly score $s_{i,0}^m$ in these memory bank-based methods [7].

C. Geometric Feature Encoding

The main issue that limits the discriminative capability of $s_{i,0}^m$ in Section III-B is its isotropic nature, which ignores other critical characteristics valuable for anomaly detection. Nevertheless, local directional consistency can act as an auxiliary property to quantitatively evaluate the normality of target samples: Features aligned with the principal directions of normal samples within the local feature spaces are expected to demonstrate a higher degree of normality.

Therefore, a geometric encoding operator $\mathcal{E}(\cdot)$ that naturally characterizes the first-order local distribution within the local manifold centered at $\mathbf{m}_{i,j}^m$ can be defined as [22]:

$$\begin{aligned} (\mathbf{m}_{i,j}^m, \mathbf{d}_{i,j}^m, s_{i,j}^m) &= \mathcal{E}_{\mathbf{m}_{i,j}^m}(\mathbf{f}_i^m), \\ s_{i,j}^m &= \|\mathbf{f}_i^m - \mathbf{m}_{i,j}^m\|, \quad \mathbf{d}_{i,j}^m = (\mathbf{f}_i^m - \mathbf{m}_{i,j}^m)/s_{i,j}^m, \end{aligned} \quad (1)$$

where $s_{i,j}^m$ represents the Euclidean distance and $\mathbf{d}_{i,j}^m$ denotes the directional vector. Moreover, Eq. (1) is a seamless encoding of \mathbf{f}_i^m . This property enables the preservation of complete details for the subsequent learning process, avoiding comprising valuable information in feature adaptation frameworks [6], [9].

D. Anisotropic Local Distance Metric

Based on Eq. (1), we aim to learn a unified metric $l(\mathbf{f}_i^P, \mathbf{f}_i^R, \mathbf{m}_{i,j}^P, \mathbf{m}_{i,j}^R)$ for multimodal anomaly detection that outperforms the Euclidean distances $s_{i,j}^P$ and $s_{i,j}^R$. While existing local metric learning methods [23], [24] use instance-dependent Mahalanobis distances, they are computationally expensive and unsuitable for our high-dimensional joint feature space (1920 dimensions). From the perspective of spectral analysis, Mahalanobis distances determine the scaling factors along principle directions. Mimicking this desired property, we propose the LSPN that leverages a neural network for computational efficiency and implicitly captures shared information across local spaces.

Specifically, LSPN predicts direction-aware scaling factors $w_{i,j}^m$ via a simple Multilayer Perceptron $\Phi(\cdot)$ (MLP) as:

$$[w_{i,j}^P, w_{i,j}^R] = \Phi(\mathbf{m}_{i,j}^P, \mathbf{m}_{i,j}^R, \mathbf{d}_{i,j}^P, \mathbf{d}_{i,j}^R). \quad (2)$$

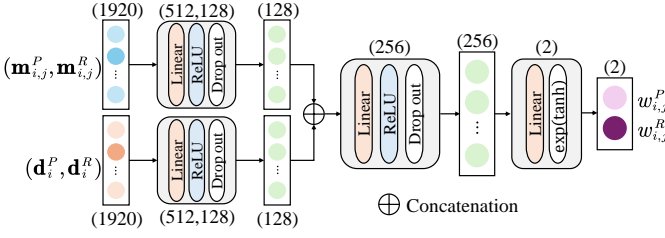


Fig. 4. The architecture of LSPN. Each block contains a linear layer, ReLU activation, and dropout. The final layer activation is a $\exp(\tanh(\cdot))$ function that is symmetrical to one and serves as scale suppression/amplification.

Furthermore, the anisotropic metric $l(\cdot)$ is defined in terms of these scaling factors as:

$$l_{i,j} = l(\mathbf{f}_i^P, \mathbf{f}_i^R, \mathbf{m}_{i,j}^P, \mathbf{m}_{i,j}^R) = \sum_{m \in \{P,R\}} w_{i,j}^m s_{i,j}^m \sigma^m, \quad (3)$$

where σ^m is a *trainable global* scaling factor that describes the influence of modality m . Eq. (3) demonstrates that $l(\cdot)$ incorporates structural priors from unimodal anomaly detection, where $s_{i,0}^m$ explicitly represents the unimodal anomaly score. When initializing Φ with $w_{i,j}^m \approx 1$, the metric $l(\cdot)$ originates as a Euclidean measure in the joint feature space. Although this baseline configuration is marginally effective in unimodal scenarios, it progressively evolves into an anisotropic metric during training under the regularization of $s_{i,j}^m$. This unique property prevents overfitting that would occur when learning a metric entirely from scratch [10], [11]. Furthermore, the supplementary material tracks model performance throughout different training epochs, revealing that G²SF attains competitive performance within remarkably few training epochs that benefit from the above design.

The architecture of $\Phi(\cdot)$ is illustrated in Fig. 4, which consists of two parallel branches that independently concatenate and encode the prototypes $(\mathbf{m}_{i,j}^P, \mathbf{m}_{i,j}^R)$ and directions $(\mathbf{d}_{i,j}^P, \mathbf{d}_{i,j}^R)$. $w_{i,j}^m$ is outputted through an activation $\exp(\tanh(\cdot))$ at the final layer, ensuring $w_{i,j}^m \in [e^{-1}, e^1]$. This constrains the scaling factors to be symmetric around the Euclidean baseline ($w_{i,j}^m = 1$). To enhance the discriminative power of $l(\cdot)$, we aim to reduce scales ($w_{i,j}^m < 1$) for normal samples, while increasing scales ($w_{i,j}^m > 1$) for anomalous samples.

E. Loss Functions

Due to the lack of anomalous samples, the predicted $w_{i,j}^m$ will converge to e^{-1} during training, yielding trivial direction-invariant $l(\cdot)$. We address this through synthetic anomaly injection in Section III-G. We denote the label $y_i \in \{0, 1\}$ for $(\mathbf{f}_i^P, \mathbf{f}_i^R)$, where $y_i = 1$ denotes synthetic anomalies. Additionally, we denote $(\cdot)_+$ as $\max(\cdot, 0)$.

1) *Discrimination Loss*: This loss aims to promote the discrepancy of learned metric values $l(\cdot)$ between normal ($y_i = 0$) and anomalous ($y_i = 1$) samples. Moreover, we prioritize $l_{i,0}$ to inherit its discriminative capability with respect to the nearest prototype $\mathbf{m}_{i,0}^m$.

Separation Loss: In line with the semi-supervised anomaly detection framework proposed in [25], the separation loss \mathcal{L}_{sep}

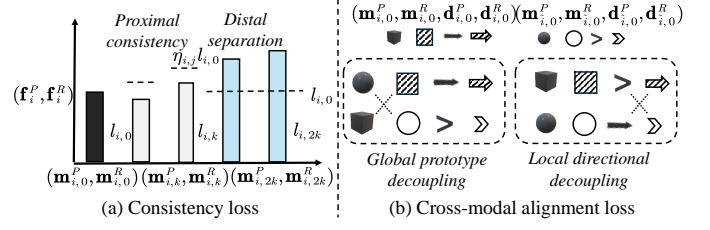


Fig. 5. (a) **Consistency loss** \mathcal{L}_{cns} , where *Proximal consistency* enforces an upper bound on $l_{i,j}^k$ to ensure metric continuity, and *Distal separation* imposes a lower bound on $l_{i,j}^{2k}$ to avoid incredible values. (b) **Cross-modal alignment loss** \mathcal{L}_{cma} , where we disentangle cross-modal correspondences between prototypes and directions from a global-to-local granularity.

is designed to enforce the minimization of metric values for normal samples while simultaneously maximizing them for anomalous instances, formally expressed as:

$$\mathcal{L}_{sep} = \sum_i (1 - y_i) l_{i,0} + y_i (l_{i,0}^{-1} - m_0^{-1})_+, \quad (4)$$

where the threshold m_0 prevents excessively large anomaly scores by setting $m_0 = 2 \max_{i,m} s_{i,0}^m$ among all training samples, ensuring numerical stability.

Margin Loss: To address the boundary ambiguity issue not explicitly considered by \mathcal{L}_{sep} , the margin loss \mathcal{L}_{mar} mitigates the distribution overlap between normal and anomalous samples, adapted from [26]:

$$\mathcal{L}_{mar} = \frac{1}{m_u} \sum_i \underbrace{(1 - y_i)(l_{i,0} - m_l)_+}_{\text{Overlap of Normal Part}} + \underbrace{y_i(m_u - l_{i,0})_+}_{\text{Overlap of Anomalous Part}}, \quad (5)$$

where $m_l = \min_{i|y_i=1} l_{i,0}$ is the lower bound of $l_{i,0}$ for anomalous samples and $m_u = \max_{i|y_i=0} l_{i,0}$ is the upper bound for normal samples. m_l and m_u are computed in a batch-wise.

2) *Geometry-Preserved Loss*: Since learning a robust and generalizable $l(\cdot)$ in the high-dimensional space for anomaly detection is challenging, despite the architecture design in Section III-D, we aim to exploit the desired geometric properties of $l(\cdot)$ that benefit our task.

Consistency Loss: Eqs. (4) and (5) concern on the discriminative power of $l_{i,0}$, critical behaviors of $l_{i,j}$ across different local spaces around $\mathbf{m}_{i,j}^m$ remain unexploited. Incorporating $l_{i,j}$ serves two critical purposes: (i) Spatial regularization that stabilizes metric learning. (ii) Data augmentation that effectively increases sample diversity within each local space through multi-prototype observations. Specifically, we promote the following two properties of geometric consistency, as illustrated in Fig. 5:

- *Proximal consistency*: $l(\cdot)$ is continuous across neighborhood. For adjacent local spaces, i.e., $1 \leq j \leq k$, $l_{i,j}$ is upper bounded by $\eta_{i,j} l_{i,0}$ for $\eta_{i,j} > 1$. It means that the partial gradient of $l(\cdot)$ w.r.t. $(\mathbf{m}_{i,j}^P, \mathbf{m}_{i,j}^R)$ is limited.
- *Distal separation*: For sufficiently large Euclidean distances, $l(\cdot)$ should maintain correspondingly significant values. We mandate $l_{i,j}$ in distant local spaces indexed by $k+1 \leq j \leq 2k$ lower-bounded by $l_{i,0}$. This constraint prevents metric collapse in high-dimensional spaces to avoid incredible values.

With the above purposes, \mathcal{L}_{cns} is formulated as:

$$\mathcal{L}_{cns} = \frac{1}{k} \sum_i \underbrace{\sum_{1 \leq j \leq k} (l_{i,j} - \eta_{i,j} l_{i,0})_+}_{\text{Proximal Consistency}} + \underbrace{\sum_{k+1 \leq j \leq 2k} (l_{i,0} - l_{i,j})_+}_{\text{Distal Separation}}. \quad (6)$$

We set $\eta_{i,j} = \eta_0 \cdot (\sum_m s_{i,j}^m) / (\sum_m s_{i,0}^m)$ proportional to the original Euclidean distances.

Scaling Loss: Despite $l(\cdot)$, we aim to encourage $w_{i,0}^m$ to encode local directional distributions explicitly, that is, suppress/amplify for normal/anomalous samples. To achieve this, we propose an asymmetric scaling loss:

$$\mathcal{L}_{sc} = \sum_i \sum_{m \in \{P,R\}} (1 - y_i)(w_{i,0}^m - 1)_+ + y_i(e^1 - w_{i,0}^m). \quad (7)$$

\mathcal{L}_{sc} asymmetrically compresses scaling factors of normal samples while anchoring synthetic anomalies near the upper limit (e^1). This design is motivated by the observation that synthetic anomalies exhibit more pronounced deviations than real-world anomalies. Consequently, their penalization in \mathcal{L}_{sc} is more aggressive.

Cross-modal Alignment Loss: So far, the prototypes (directions) of two modalities have been naively concatenated as input to LSPN in Section III-D, not considering cross-modal geometric alignments. To address it, we propose a simple yet effective strategy by disentangling cross-modal correspondences between prototypes and directions.

Specifically, by permuting indices $\{i\} \rightarrow \{\tilde{i}\}$, we can construct two kinds of negative samples, as illustrated in Fig. 5:

$$(\mathbf{m}_{i,0}^P, \mathbf{m}_{\tilde{i},0}^R, \mathbf{d}_{i,0}^P, \mathbf{d}_{\tilde{i},0}^R), (\mathbf{m}_{i,0}^R, \mathbf{m}_{\tilde{i},0}^P, \mathbf{d}_{i,0}^R, \mathbf{d}_{\tilde{i},0}^P). \quad (8)$$

The latter focuses on capturing discordant directions while maintaining prototype consistency at a local structural granularity; in contrast, the former prioritizes holistic prototype coherence through a global structural perspective.

During training, we construct the two kinds of negative samples with equal probability. Denote $\tilde{w}_{i,0}^m$ ($m \in \{P,R\}$) as the scaling factors corresponding to these negative samples, we define the cross-modal alignment loss as:

$$\mathcal{L}_{cma} = \sum_i \sum_{m \in \{P,R\}} (e^1 - \tilde{w}_{i,0}^m), \quad (9)$$

which enforces large scales similar to synthetic anomalous samples in Eq. (7).

3) *Overall Loss:* Finally, the overall loss \mathcal{L} of our G²SF framework combines all terms as:

$$\mathcal{L} = \underbrace{\mathcal{L}_{sep} + \alpha \mathcal{L}_{mar}}_{\text{Discrimination Loss}} + \underbrace{\beta \mathcal{L}_{cns} + \gamma \mathcal{L}_{sc} + \mu \mathcal{L}_{cma}}_{\text{Geometry-Preserved Loss}}, \quad (10)$$

where α , β , γ , and μ are hyper-parameters balancing the loss components.

F. Geometry-Informed Anomaly Scoring

During inference, G²SF computes the anomaly score s_i for each multimodal feature pair $(\mathbf{f}_i^P, \mathbf{f}_i^R)$. Concretely, by propagating features through the geometric encoding operator

and LSPN, we obtain the anisotropic metrics $\{l_{i,j}\}_{j=0}^k$ across $k+1$ nearest local spaces, adhering to the proximal consistency constraint in Eq. (6). We apply a min operator to aggregate $\{l_{i,j}\}_{j=0}^k$ to define s_i :

$$s_i = \min\{l_{i,j} | j = 0, 1, \dots, k\}. \quad (11)$$

This definition stems from a geometric prior. Specifically, memory bank-based methods calculate anomaly scores using Euclidean distances to their memory banks (Section III-B), whereas our formulation in Eq. (11) reformulates this as distance measurement to the normal data manifold through the anisotropic metrics $l(\cdot)$. We will compare Eq. (11) with several alternatives in Section IV-C.

Finally, the sample-level anomaly score is obtained by taking the maximum s_i across all feature pairs extracted from a test sample. Following [6], [7], [18], we apply bilinear interpolation and a Gaussian kernel with size 4 to upsample and smooth the score map, ensuring resolution alignment with input dimensions.

G. Anomaly Synthesis

Our anomaly synthesis procedure operates following Cut-Paste approaches [8], [27], [28]: First, we generate Berlin noise maps, which are binarized into mask maps to select paste locations. Based on these masks, we then cut corresponding regions from source (normal) 3D point clouds and RGB images from the training dataset. The source point clouds can be other classes or more general 3D models. Subsequently, we apply random augmentations to corrupt the regions - specifically implementing pixel modifications for source images [27], e.g., distortion, brightness, and sharpness changes, while executing random translations for source point clouds. The corrupted regions are finally pasted onto target data. Examples of synthetic anomalous samples are provided in the supplementary material.

IV. EXPERIMENT

A. Experimental Details

Dataset: Experiments are conducted on the MVTEC-3D AD dataset [2] containing 10 industrial object categories. Training data comprises 210–361 samples per class (total 2,656), while testing data contains 69–132 samples per class (total 249). Each sample provides aligned RGB images and 3D point clouds, enabling pixel-wise correspondence between color and spatial coordinates.

Evaluation Metrics: We assess the image-level anomaly detection performance by the Area Under the Receiver Operator Curve (I-AUROC). For evaluating the pixel-wise anomaly segmentation, we adopt the pixel-level AUROC (P-AUROC) and the Area Under the Per-Region Overlap (AUPRO) at 30% integration limits (denoted as AUPRO@30%), the same as existing methods [3], [7], [18], [19]. To better demonstrate the advantages of our method in practical industrial scenarios, particularly its low false positive rate and better recall, we have additionally introduced the AUPRO@1% metric used in recent studies [18], [19].

	Method	Bagel	Cable Gland	Carrot	Cookie	Dowel	Foam	Peach	Potato	Rope	Tire	Mean
I-AUROC	DepthGAN [2]	0.538	0.372	0.580	0.603	0.430	0.534	0.642	0.601	0.443	0.577	0.532
	VoxelGAN [2]	0.680	0.324	0.565	0.399	0.497	0.482	0.566	0.579	0.601	0.482	0.517
	BTF [3]	0.918	0.748	0.967	0.883	0.932	0.582	0.896	0.912	0.921	0.886	0.865
	EasyNet [8]	0.991	0.998	0.918	0.968	0.945	0.945	0.905	0.807	<u>0.994</u>	0.793	0.926
	AST [29]	0.983	0.873	0.976	0.971	0.932	0.885	0.974	0.981	1.000	0.797	0.937
	M3DM [7]	0.994	0.909	0.972	0.976	0.960	0.942	0.973	0.899	0.972	0.850	0.945
	Shape-guided [19]	0.986	0.894	0.983	0.991	0.976	0.857	0.990	0.965	0.960	0.869	0.947
	CFM [18]	0.994	0.888	<u>0.984</u>	0.993	0.980	0.888	0.941	0.943	0.980	0.953	<u>0.954</u>
	LSFA [6]	1.000	<u>0.939</u>	0.982	0.989	0.961	<u>0.951</u>	0.983	0.962	0.989	<u>0.951</u>	0.971
	Ours	0.997	0.923	0.993	0.967	0.966	0.991	0.994	0.988	0.966	0.922	0.971
AUPRO@30%	DepthGAN [2]	0.421	0.422	0.778	0.696	0.494	0.252	0.285	0.362	0.402	0.631	0.474
	VoxelGAN [2]	0.664	0.620	0.766	0.740	0.783	0.332	0.582	0.790	0.633	0.483	0.639
	BTF [3]	0.976	0.969	0.979	0.973	0.933	0.888	0.975	0.981	0.950	0.971	0.959
	AST [29]	0.970	0.947	<u>0.981</u>	0.939	0.913	0.906	0.979	<u>0.982</u>	0.889	0.940	0.944
	M3DM [7]	0.970	0.971	<u>0.979</u>	0.950	0.941	0.932	0.977	<u>0.971</u>	0.971	0.975	0.964
	Shape-guided [19]	0.981	0.973	0.982	0.971	<u>0.962</u>	0.978	0.981	0.983	0.974	0.975	0.976
	CFM [18]	0.979	0.972	0.982	0.945	<u>0.950</u>	0.968	0.980	<u>0.982</u>	<u>0.975</u>	<u>0.981</u>	0.971
	LSFA [6]	0.986	<u>0.974</u>	<u>0.981</u>	0.946	0.925	0.941	0.983	0.983	0.974	0.983	0.968
	Ours	<u>0.982</u>	0.976	0.982	0.979	0.971	<u>0.976</u>	<u>0.982</u>	0.983	0.978	<u>0.981</u>	0.979

TABLE I

I-AUROC AND AUPRO@30% RESULTS ON MVTEC-3D AD. BEST RESULTS IN BOLD, RUNNER-UPS UNDERLINED.

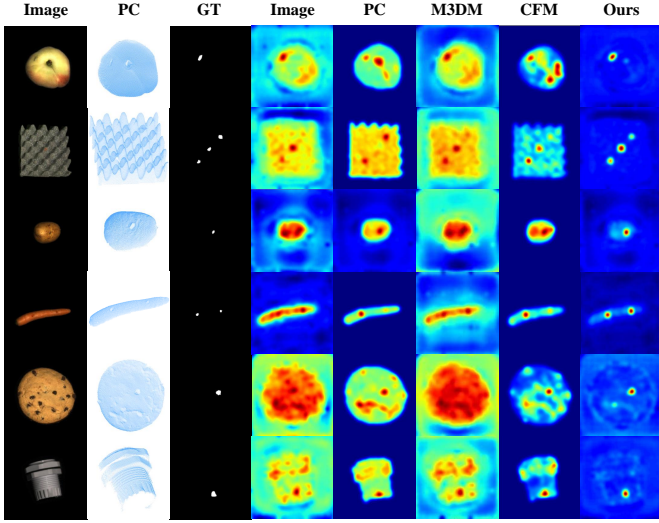


Fig. 6. Qualitative comparison on MVTEC-3D AD [2]: Visualized results include original RGB images with aligned 3D point clouds (PC) and ground truths (GT), alongside anomaly detection outputs from unimodal methods (PatchCore [5] for image/point cloud) and multimodal benchmarks (M3DM [7], CFM [18]), compared against our proposed G^2SF framework.

Method	I-AUROC	P-AUROC	AUPRO @30%	AUPRO @1%
BTF [3]	0.865	0.992	0.959	0.383
AST [29]	0.937	0.976	0.944	0.398
M3DM [7]	0.945	0.992	0.964	0.394
Shape-guided [18]	0.947	<u>0.996</u>	<u>0.976</u>	<u>0.456</u>
CFM [18]	<u>0.954</u>	0.993	0.971	0.455
LSFA [6]	0.971	0.993	0.968	-
Ours	0.971	0.997	0.979	0.468

TABLE II

MEAN METRICS FOR ALL CATEGORIES OF MVTEC-3D AD.

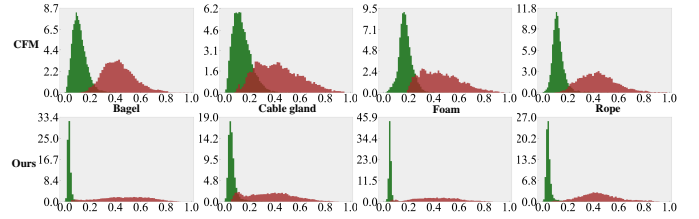


Fig. 7. Pixel-wise anomaly score distributions in *Bagel*, *Cable gland*, *Foam*, and *Rope* categories, where the horizontal axis is normalized anomaly score (0-1) and the vertical axis is the probability density. Green/Brown distributions represent normal/anomalous regions respectively. Compared with CFM [18] (top), our method (bottom) achieves significant distribution compression in normal regions while maintaining anomaly discrimination.

Score	I-AUROC	P-AUROC	AUPRO@30%	AUPRO@1%
s_i^R	0.849	0.988	0.947	0.363
s_i^P	0.854	0.975	0.915	0.319
$w_{i,0}^R$	0.916	0.948	0.916	0.439
$w_{i,0}^P$	0.915	0.984	0.958	0.443
s_i	0.971	0.997	0.979	0.468

TABLE III

ANALYSIS OF VARIOUS SCORE METRICS FOR ANOMALY DETECTION.

Components	Stepwise Combinations				
\mathcal{L}_{sep} in Eq. (4)	✓	✓	✓	✓	✓
\mathcal{L}_{cns} in Eq. (6)	✗	✓	✓	✓	✓
\mathcal{L}_{mar} in Eq. (5)	✗	✗	✓	✓	✓
\mathcal{L}_{sc} in Eq. (7)	✗	✗	✗	✓	✓
\mathcal{L}_{cma} in Eq. (9)	✗	✗	✗	✗	✓
I-AUROC	0.868	0.950	0.950	0.961	0.971
P-AUROC	0.994	0.995	0.996	0.997	0.997
AUPRO@30%	0.967	0.972	0.975	0.978	0.979

TABLE IV

ABLATION RESULTS OF INDIVIDUAL LOSS COMPONENTS WITHIN G^2SF .

Implementation: We follow a similar procedure of M3DM [7] for feature extraction and preprocessing of the dataset. For the consistency loss \mathcal{L}_{cns} , we set $k = 5$ and $\eta_0 = 1.2$. The tuning parameters associated with each loss are set as $\alpha =$

$10, \beta = 60, \gamma = 8, \mu = 20$. We train our G^2SF with the Adam optimizer [30] with 80 epochs and batch size 8192. More details are provided in the supplementary material.

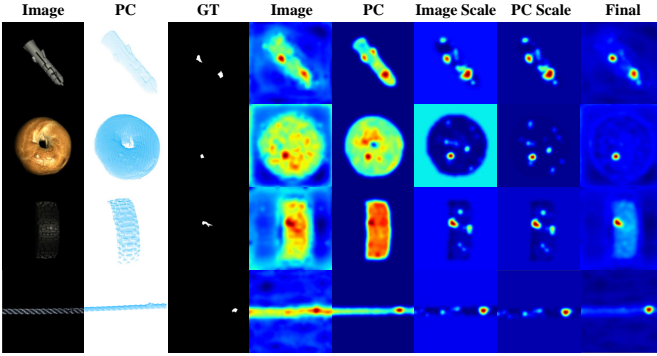


Fig. 8. Qualitative result on MVTEC-3D AD: Original RGB images, 3D point clouds (PC), ground truth (GT), and score maps of s_i^R (Image), s_i^P (PC), $w_{i,0}^R$ (Image Scale), $w_{i,0}^P$ (PC Scale), and s_i (Final), from left to right. The scaling factors ($w_{i,0}^R, w_{i,0}^P$) exhibit false positives in certain normal regions, whereas the final score s_i effectively suppresses these errors through incorporating distance information from s_i^R and s_i^P .

B. Comparison on Multimodal Benchmarks

We illustrate the results of I-AUROC and AUPRO@30% in Table I, while those of AUPRO@1% and P-AUROC are presented in Table II. Specifically, for anomaly detection, the proposed G²SF achieves the highest I-AUROC value of 97.1%. Although LSFA [6] matches G²SF in terms of I-AUROC, its AUPRO@30% result for anomaly segmentation is 96.8%, which is lower than G²SF’s 97.9%. Regarding anomaly segmentation, our G²SF outperforms all competitors in three pixel metrics with a +1.2% AUPRO@1% advantage over Shape-guided [19]. Notably, for AUPRO@30% value, although Shape-guided is close to G²SF, its I-AUROC of 94.7% is significantly lower than G²SF’s 97.1%. Overall, G²SF achieves the best performance in both anomaly detection and anomaly segmentation tasks. This performance gain stems from our purpose of learning a discriminative local distance metric. As demonstrated by the qualitative results visualized in Fig. 6, G²SF effectively suppresses overestimated scores in normal regions compared to M3DM [7] and CFM [18], while producing sharper anomaly boundaries. To provide a comprehensive visualization, Fig. 7 illustrates pixel-wise anomaly score distributions in four categories, demonstrating that anomaly scores of normal regions in G²SF shrinkage significantly within a narrow range. This property effectively reduces false positives, leading to more substantial gains in AUPRO@1% (Table II). More qualitative results are provided in the supplementary material.

C. Analysis

Effectiveness of Final Score s_i : Table III compares key score metrics for anomaly detection: unimodal scores s_i^m ($m \in \{P, R\}$) (Euclidean distances, see Section III-B), scaling factors $w_{i,0}^m$ from LSPN in Eq. (2), and our fused score s_i in Eq. (11). As evidenced in Table III, unimodal anomaly scores s_i^m demonstrate suboptimal performance. This limitation stems from the inherent information incompleteness of individual modalities. Our fused score s_i overcomes these constraints through cross-modal complementarity, achieving significant

Strategy	I-AUROC	P-AUROC	AUPRO@30%	AUPRO@1%
$l_{i,0}$	0.963	0.997	0.977	0.461
max	0.953	0.986	0.960	0.453
mean	0.972	0.983	0.955	0.458
min	0.971	0.997	0.979	0.468

TABLE V
INVESTIGATION ON DIFFERENT SCORE AGGREGATION STRATEGIES.

improvements over unimodal baselines. These quantitative gains are also supported by Figs. 6 and 8.

While $w_{i,0}^m$ characterizes the local directions of normal features within local spaces (Section III-D), its exclusion of the valuable distances, i.e., s_i^m , leads to critical limitations. Specifically, proximity to memory prototypes ($s_i^m \rightarrow 0$) inherently indicates normality regardless of directional deviations, which is a prior ignored by $w_{i,0}^m$. As evidenced in Fig. 8, the score maps obtained by $w_{i,0}^m$ exhibit noticeable false positives. Using s_i in our G²SF mitigates this issue, which benefits from sufficiently leveraging complementary directional and distance information. The comprehensive results of all categories are provided in the supplementary material.

Ablation of Individual Loss Components: Table IV systematically evaluates the contribution of each loss component through stepwise removal. Using the separation loss \mathcal{L}_{sep} as the baseline for the metric learning, the addition of the consistency loss \mathcal{L}_{cns} drives an 8.2% I-AUROC improvement, surpassing M3DM [7] across all metrics and achieving parity with CFM [18]. The margin loss \mathcal{L}_{mar} specifically improves pixel-wise localization (AUPRO@30% +0.3%), while the scaling loss \mathcal{L}_{sc} and cross-modal alignment loss \mathcal{L}_{cma} further enhances image-level detection (I-AUROC +1.1/1.0%). These synergistic effects collectively establish G²SF’s state-of-the-art performance, validating the necessity of all proposed loss components.

Investigation of Score Aggregation Strategy: Section III-F employs a min operator in Eq. (11) to aggregate metrics $\{l_{i,j}\}$ from adjacent local spaces. We systematically evaluate three alternatives in Table V: (1) single-space baseline $l_{i,0}$. (2) max operator. (3) mean operator. The min-based strategy achieves superior overall performance (+0.8%/0.7% I-AUROC/AUPRO@1% vs $l_{i,0}$), validating the necessity of multi-space consensus. While max and mean operators incorporate adjacent local spaces, they indiscriminately weight less discriminative $l_{i,j}$ from distant regions, compromising detection precision. The min operator in Eq. (11) prioritizes the most representative local metric through a proper geometric prior as discussed in Section III-F. The results of all categories of MVTEC-3D AD are summarized in the supplementary material.

V. CONCLUSION

In this paper, we propose G²SF for multimodal anomaly detection, which learns a unified anisotropic local distance metric to replace the indiscriminative isotropic Euclidean metrics. This metric is formulated by the direction-aware scaling factors predicted by LSPN and original Euclidean distances in individual modalities. We propose new loss functions to enable robust metric learning, serving for discrimination or

geometric property maintenance. A geometric prior-induced anomaly scoring strategy is proposed to enhance anomaly detection and segmentation. Extensive experimental results show our superior performance with low positive rate and better recall compared to existing state-of-the-art methods.

REFERENCES

- [1] P. Bergmann, M. Fauser, D. Sattlegger, and C. Steger, "MVTec AD-a comprehensive real-world dataset for unsupervised anomaly detection," in *Proceedings of the IEEE/CVF Conference on Computer Vision and Pattern Recognition*, 2019, pp. 9592–9600.
- [2] P. Bergmann, X. Jin, D. Sattlegger, and C. Steger, "The MVTec-3D AD dataset for unsupervised 3D anomaly detection and localization," *arXiv preprint arXiv:2112.09045*, 2021.
- [3] E. Horwitz and Y. Hoshen, "Back to the feature: classical 3D features are (almost) all you need for 3D anomaly detection," in *Proceedings of the IEEE/CVF Conference on Computer Vision and Pattern Recognition*, 2023, pp. 2968–2977.
- [4] Y. Guo, M. Jiang, Q. Huang, Y. Cheng, and J. Gong, "Mldfr: A multilevel features restoration method based on damaged images for anomaly detection and localization," *IEEE Transactions on Industrial Informatics*, vol. 20, no. 2, pp. 2477–2486, 2023.
- [5] K. Roth, L. Pemula, J. Zepeda, B. Schölkopf, T. Brox, and P. Gehler, "Towards total recall in industrial anomaly detection," in *Proceedings of the IEEE/CVF Conference on Computer Vision and Pattern Recognition*, 2022, pp. 14 318–14 328.
- [6] Y. Tu, B. Zhang, L. Liu, Y. Li, J. Zhang, Y. Wang, C. Wang, and C. Zhao, "Self-supervised feature adaptation for 3D industrial anomaly detection," in *European Conference on Computer Vision*. Springer, 2024, pp. 75–91.
- [7] Y. Wang, J. Peng, J. Zhang, R. Yi, Y. Wang, and C. Wang, "Multimodal industrial anomaly detection via hybrid fusion," in *Proceedings of the IEEE/CVF Conference on Computer Vision and Pattern Recognition*, 2023, pp. 8032–8041.
- [8] R. Chen, G. Xie, J. Liu, J. Wang, Z. Luo, J. Wang, and F. Zheng, "Easynet: An easy network for 3d industrial anomaly detection," in *Proceedings of the 31st ACM International Conference on Multimedia*, 2023, pp. 7038–7046.
- [9] T. Reiss, N. Cohen, L. Bergman, and Y. Hoshen, "Panda: Adapting pretrained features for anomaly detection and segmentation," in *Proceedings of the IEEE/CVF Conference on Computer Vision and Pattern Recognition*, 2021, pp. 2806–2814.
- [10] J. Fan, Y. Feng, and X. Tong, "A road to classification in high dimensional space: the regularized optimal affine discriminant," *Journal of the Royal Statistical Society Series B: Statistical Methodology*, vol. 74, no. 4, pp. 745–771, 2012.
- [11] J. Fan, Y. Fan, and Y. Wu, "High-dimensional classification," in *High-Dimensional Data Analysis*. World Scientific, 2011, pp. 3–37.
- [12] J. Pirnay and K. Chai, "Inpainting transformer for anomaly detection," in *International Conference on Image Analysis and Processing*. Springer, 2022, pp. 394–406.
- [13] J. Wyatt, A. Leach, S. M. Schmon, and C. G. Willcocks, "Anoddpn: Anomaly detection with denoising diffusion probabilistic models using simplex noise," in *Proceedings of the IEEE/CVF Conference on Computer Vision and Pattern Recognition*, 2022, pp. 650–656.
- [14] T. Defard, A. Setkov, A. Loesch, and R. Audigier, "PaDiM: a patch distribution modeling framework for anomaly detection and localization," in *International Conference on Pattern Recognition*. Springer, 2021, pp. 475–489.
- [15] D. Gudovskiy, S. Ishizaka, and K. Kozuka, "CFLOW-AD: Real-time unsupervised anomaly detection with localization via conditional normalizing flows," in *Proceedings of the IEEE/CVF Winter Conference on Applications of Computer Vision*, 2022, pp. 98–107.
- [16] J. Bae, J.-H. Lee, and S. Kim, "PNI: industrial anomaly detection using position and neighborhood information," in *Proceedings of the IEEE/CVF International Conference on Computer Vision*, 2023, pp. 6373–6383.
- [17] X. Jiang, J. Liu, J. Wang, Q. Nie, K. Wu, Y. Liu, C. Wang, and F. Zheng, "Softpatch: Unsupervised anomaly detection with noisy data," *Advances in Neural Information Processing Systems*, vol. 35, pp. 15 433–15 445, 2022.
- [18] A. Costanzino, P. Z. Ramirez, G. Lisanti, and L. Di Stefano, "Multimodal industrial anomaly detection by crossmodal feature mapping," in *Proceedings of the IEEE/CVF Conference on Computer Vision and Pattern Recognition*, 2024, pp. 17 234–17 243.
- [19] Y.-M. Chu, C. Liu, T.-I. Hsieh, H.-T. Chen, and T.-L. Liu, "Shape-guided dual-memory learning for 3D anomaly detection," in *Proceedings of the 40th International Conference on Machine Learning*, 2023.
- [20] M. Caron, H. Touvron, I. Misra, H. Jégou, J. Mairal, P. Bojanowski, and A. Joulin, "Emerging properties in self-supervised vision transformers," in *Proceedings of the IEEE/CVF International Conference on Computer Vision*, 2021, pp. 9650–9660.
- [21] Y. Pang, W. Wang, F. E. Tay, W. Liu, Y. Tian, and L. Yuan, "Masked autoencoders for point cloud self-supervised learning," in *European Conference on Computer Vision*. Springer, 2022, pp. 604–621.
- [22] Y. Zhou, X. Song, Y. Zhang, F. Liu, C. Zhu, and L. Liu, "Feature encoding with autoencoders for weakly supervised anomaly detection," *IEEE Transactions on Neural Networks and Learning Systems*, vol. 33, no. 6, pp. 2454–2465, 2021.
- [23] J. Wang, A. Kalousis, and A. Woznica, "Parametric local metric learning for nearest neighbor classification," *Advances in Neural Information Processing Systems*, vol. 25, 2012.
- [24] H.-J. Ye, D.-C. Zhan, N. Li, and Y. Jiang, "Learning multiple local metrics: Global consideration helps," *IEEE Transactions on Pattern Analysis and Machine Intelligence*, vol. 42, no. 7, pp. 1698–1712, 2019.
- [25] L. Ruff, R. A. Vandermeulen, N. Görnitz, A. Binder, E. Müller, K.-R. Müller, and M. Kloft, "Deep semi-supervised anomaly detection," in *International Conference on Learning Representations*, 2020. [Online]. Available: <https://openreview.net/forum?id=HkgHOTEYwH>
- [26] Y. Cao, X. Xu, Z. Liu, and W. Shen, "Collaborative discrepancy optimization for reliable image anomaly localization," *IEEE Transactions on Industrial Informatics*, vol. 19, no. 11, pp. 10 674–10 683, 2023.
- [27] X. Yao, R. Li, J. Zhang, J. Sun, and C. Zhang, "Explicit boundary guided semi-push-pull contrastive learning for supervised anomaly detection," in *Proceedings of the IEEE/CVF Conference on Computer Vision and Pattern Recognition*, 2023, pp. 24 490–24 499.
- [28] C.-L. Li, K. Sohn, J. Yoon, and T. Pfister, "Cutpaste: Self-supervised learning for anomaly detection and localization," in *Proceedings of the IEEE/CVF Conference on Computer Vision and Pattern Recognition*, 2021, pp. 9664–9674.
- [29] M. Rudolph, T. Wehrbein, B. Rosenhahn, and B. Wandt, "Asymmetric student-teacher networks for industrial anomaly detection," in *Proceedings of the IEEE/CVF Winter Conference on Applications of Computer Vision*, 2023, pp. 2592–2602.
- [30] D. P. Kingma and J. Ba, "Adam: A method for stochastic optimization," *arXiv preprint arXiv:1412.6980*, 2014.
- [31] J. Deng, W. Dong, R. Socher, L.-J. Li, K. Li, and L. Fei-Fei, "Imagenet: A large-scale hierarchical image database," in *2009 IEEE Conference on Computer Vision and Pattern Recognition*. Ieee, 2009, pp. 248–255.
- [32] A. X. Chang, T. Funkhouser, L. Guibas, P. Hanrahan, Q. Huang, Z. Li, S. Savarese, M. Sava, S. Song, H. Su *et al.*, "Shapenet: An information-rich 3d model repository," *arXiv preprint arXiv:1512.03012*, 2015.
- [33] K. He, X. Zhang, S. Ren, and J. Sun, "Delving deep into rectifiers: Surpassing human-level performance on imagenet classification," in *Proceedings of the IEEE International Conference on Computer Vision*, 2015, pp. 1026–1034.

A. ANOMALY SYNTHESIS

The whole procedure of our cutPaste anomaly synthesis is illustrated in Fig. 1. More generated anomalous RGB images and associated 3D point clouds are provided in Fig. 4. The synthetic anomalies are pronounced than real-world anomalies in MVTEC-3D AD.

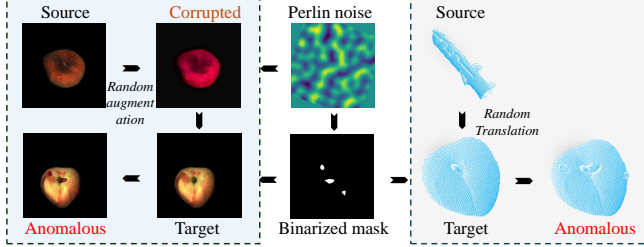


Fig. 1. Flowchart of the anomaly synthesis procedure based on CutPaste: (1) Berlin noise maps are binarized into masks to select paste locations; (2) Source regions from normal 3D point clouds/RGB images (or generic models) are cut; (3) Random corruptions (pixel/geometry augmentations) are applied; (4) Modified regions are pasted onto target data.

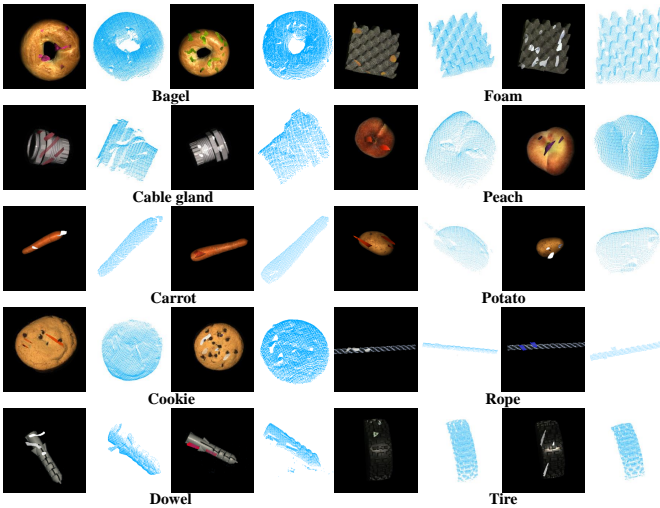


Fig. 2. Visualization of generated anomalous RGB images and 3D point clouds on MVTEC-3D AD.

B. IMPLEMENTATION DETAILS

A. Feature Extraction

RGB features are extracted using DINO ViT-B/8 [20] pretrained on ImageNet [31], generating $28 \times 28 \times 768$ feature maps upsampled to $56 \times 56 \times 768$. Point clouds are processed via Point-MAE [21] pretrained on ShapeNet [32], grouping 3D points into 1024 clusters (feature dimension 1152) and interpolated to $56 \times 56 \times 1152$ for spatial alignment with image feature maps. We use PatchCore [5] to construct modality-specific memory banks with 10% coreset sampling. This procedure remains the same as M3DM [7] without any change.

B. Data Processing

To accelerate training and focus on discriminative foreground features, we pre-collect features from 800 synthetic

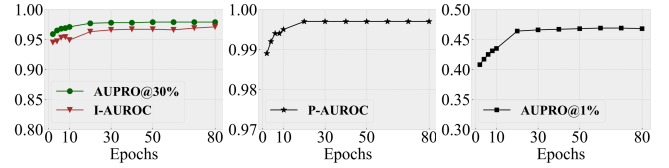


Fig. 3. Performance over different training epochs.

anomalous samples per class (Section III-G), forming a feature dataset equally split for training and validation. The features originate from foreground regions identified via RANSAC plane fitting on 3D point clouds, where areas exceeding 0.005 distance from the fitted plane are retained following [7], [18]. During evaluation on MVTEC 3D-AD, background regions remain included. As background features are excluded during training, we set their scaling factors to unity ($w_{i,0}^m = 1$) in Eq. (3), serving as a linear combination of the original unimodal results.

C. Parameter Setting

For the consistency loss \mathcal{L}_{cns} , we set $k = 5$ and $\eta_0 = 1.2$. The tuning parameters associated with each loss are set as $\alpha = 10, \beta = 60, \gamma = 8, \mu = 20$. The LSPN is trained using an Adam optimizer [30] with learning rate $1.5e^{-4}$ and weight decay $1.5e^{-4}$, combined with l_1 regularization of weight $1e^{-4}$ and drop out with ratio 0.5, over 80 epochs with a batch size of 8,192. Global scaling factors σ^m are separately optimized at a higher learning rate of $5e^{-3}$ to accelerate convergence. We initialize LSPN by the default strategy in Pytorch, that is, Kaiming Initialization [33]. We observe $w_{i,j}^m \approx 1$ under this strategy, meeting the requirement in Section III-D. For modality m , we normalize all Euclidean distances $\{s_{i,j}^m\}$ by their mean over the training dataset. Then, we initialize $\sigma^m = 0.5$ with equal importance from each modality. Finally, we implement our G²SF by Pytorch and run all experiments on Linux with Nvidia RTX 4090 GPUs.

C. LEARNING CURVE

We train multiple models that stop at $\{2,4,6,8,10,20,\dots,80\}$ epochs respectively, and report their performances (I-AUROC, P-AUROC, AUPRO@30%, and AUPRO@1%) on MVTEC-3D AD in Fig. 3. After only 4 epochs, G²SF outperforms M3DM [7] (94.5% I-AUROC, 99.2% P-AUROC, 96.4% AUPRO@30%, and 39.4% AUPRO@1%). This benefits from our design, as our model evolves from an established Euclidean metric to the target anisotropic metric, see Section III-D.

D. ADDITIONAL QUANTITATIVE RESULTS

We summarize the results of different score metrics for all categories in MVTEC-3D AD in Table I. The results demonstrate that the final score s_i outperforms unimodal scores $\{s_{i,0}^m\}$ and scaling factors $\{w_{i,0}^m\}$ almost all categories. Additionally, comprehensive quantitative results of various score aggregation operators are provided in II, which validate the superior performance of min operator over the majority of

TABLE I
RESULTS OF VARIOUS SCORE METRICS ON MVTEC-3D AD. BEST RESULTS IN **BOLD**, RUNNER-UPS UNDERLINED.

	Method	Bagel	Cable Gland	Carrot	Cookie	Dowel	Foam	Peach	Potato	Rope	Tire	Mean
I-AUROC	$s_{i,0}^R$	0.945	0.939	0.914	0.733	<u>0.939</u>	0.768	0.944	0.621	0.930	0.755	0.849
	$s_{i,0}^P$	0.951	0.637	0.981	<u>0.952</u>	<u>0.837</u>	0.786	0.923	0.930	0.858	0.688	0.854
	$w_{i,0}^R$	<u>0.969</u>	0.732	<u>0.989</u>	0.928	0.831	<u>0.983</u>	0.981	0.988	<u>0.965</u>	<u>0.798</u>	<u>0.916</u>
	$w_{i,0}^P$	<u>0.969</u>	0.727	<u>0.989</u>	0.930	0.829	<u>0.983</u>	<u>0.982</u>	0.988	0.963	0.796	0.915
	s_i	0.997	<u>0.923</u>	0.993	0.967	0.966	0.991	0.994	0.988	0.966	0.922	0.971
P-AUROC	$s_{i,0}^R$	0.992	<u>0.993</u>	0.995	<u>0.976</u>	<u>0.996</u>	0.955	0.994	0.991	0.995	<u>0.995</u>	0.988
	$s_{i,0}^P$	0.987	0.945	0.997	0.940	0.981	0.935	0.993	0.996	0.994	0.981	0.975
	$w_{i,0}^R$	0.964	0.910	0.995	0.774	0.954	0.973	0.965	0.998	0.997	0.952	0.948
	$w_{i,0}^P$	<u>0.993</u>	0.983	<u>0.998</u>	0.916	0.986	<u>0.991</u>	<u>0.995</u>	0.999	<u>0.998</u>	0.977	0.984
	s_i	0.998	0.995	0.999	0.996	0.996	0.997	0.998	0.999	0.999	0.998	0.997
AUPRO@30%	$s_{i,0}^R$	0.954	<u>0.973</u>	0.974	0.887	0.974	0.847	0.971	0.957	0.965	<u>0.970</u>	0.947
	$s_{i,0}^P$	0.96	0.806	0.977	0.899	0.929	0.761	0.971	0.976	0.946	0.927	0.915
	$w_{i,0}^R$	0.957	0.900	0.976	0.724	0.896	0.911	0.944	0.982	0.974	0.898	0.916
	$w_{i,0}^P$	<u>0.979</u>	0.953	<u>0.981</u>	<u>0.908</u>	0.934	<u>0.950</u>	<u>0.978</u>	0.983	<u>0.976</u>	0.939	<u>0.958</u>
	s_i	0.982	0.976	0.982	0.979	<u>0.971</u>	0.976	0.982	0.983	0.978	0.981	0.979
AUPRO@1%	$s_{i,0}^P$	0.367	<u>0.423</u>	0.416	0.235	0.415	0.296	0.399	0.285	0.396	0.399	0.363
	$s_{i,0}^R$	0.424	0.063	0.448	0.406	0.243	0.238	0.385	0.409	0.356	0.222	0.319
	$w_{i,0}^R$	0.480	0.384	0.480	0.378	0.356	<u>0.469</u>	0.477	0.494	<u>0.455</u>	0.416	0.439
	$w_{i,0}^P$	0.481	0.378	<u>0.481</u>	<u>0.421</u>	0.356	0.474	<u>0.480</u>	<u>0.494</u>	0.453	0.415	0.443
	s_i	0.481	0.443	0.484	0.471	<u>0.410</u>	0.468	0.487	0.499	0.468	0.471	0.468

TABLE II
RESULTS OF VARIOUS SCORE AGGREGATION STRATEGIES ON MVTEC-3D AD. BEST RESULTS IN **BOLD**, RUNNER-UPS UNDERLINED.

	Method	Bagel	Cable Gland	Carrot	Cookie	Dowel	Foam	Peach	Potato	Rope	Tire	Mean
I-AUROC	$l_{i,0}$	<u>0.997</u>	0.925	0.989	0.962	0.953	0.993	0.996	0.964	0.960	0.892	0.963
	max	0.998	<u>0.932</u>	0.982	0.966	0.949	0.968	0.999	0.862	0.953	<u>0.922</u>	0.953
	mean	<u>0.997</u>	0.940	0.988	0.975	<u>0.954</u>	0.993	0.995	0.980	0.960	0.941	0.972
	min	<u>0.997</u>	0.923	0.993	<u>0.967</u>	0.966	0.991	0.994	0.988	0.966	<u>0.922</u>	<u>0.971</u>
P-AUROC	$l_{i,0}$	<u>0.997</u>	<u>0.993</u>	0.999	<u>0.994</u>	<u>0.995</u>	0.997	0.998	0.999	0.999	0.997	0.997
	max	0.980	0.989	0.999	0.917	<u>0.993</u>	0.986	0.998	0.999	0.998	0.996	0.986
	mean	0.977	0.992	0.999	0.888	<u>0.995</u>	0.983	0.997	0.999	0.999	0.998	0.983
	min	0.998	0.995	0.999	0.996	0.996	0.997	0.998	0.999	0.999	0.998	0.997
AUPRO@30%	$l_{i,0}$	0.981	0.970	0.982	0.974	0.967	<u>0.975</u>	0.982	0.983	0.978	0.979	0.977
	max	0.968	0.960	0.982	0.883	0.954	0.936	0.982	0.983	0.976	0.974	0.960
	mean	0.965	0.970	0.982	0.815	0.961	0.932	0.982	0.983	0.978	0.979	0.955
	min	0.982	0.976	0.982	0.979	0.971	0.976	0.982	0.983	0.978	0.981	0.979
AUPRO@1%	$l_{i,0}$	0.480	0.429	0.482	<u>0.444</u>	0.411	0.467	0.485	<u>0.497</u>	<u>0.465</u>	0.448	0.461
	max	0.481	0.390	0.485	0.428	0.391	0.467	0.494	0.495	0.457	0.443	0.453
	mean	0.480	<u>0.436</u>	0.485	0.396	0.403	0.469	<u>0.491</u>	<u>0.497</u>	<u>0.465</u>	0.460	0.458
	min	0.481	0.443	0.484	0.471	<u>0.410</u>	<u>0.468</u>	<u>0.487</u>	0.499	0.468	0.471	0.468

classes, owing to its geometric interpretation, as discussed in Section III-F.

E. ADDITIONAL QUALITATIVE RESULTS

Fig. 4 provides additional qualitative results for all classes in MVTEC-3D AD. Consistent with Fig. 6, our G^2SF suppresses anomaly scores of normal regions and provides clearer anomaly boundaries, compared to M3DM [7] and CFM [18].

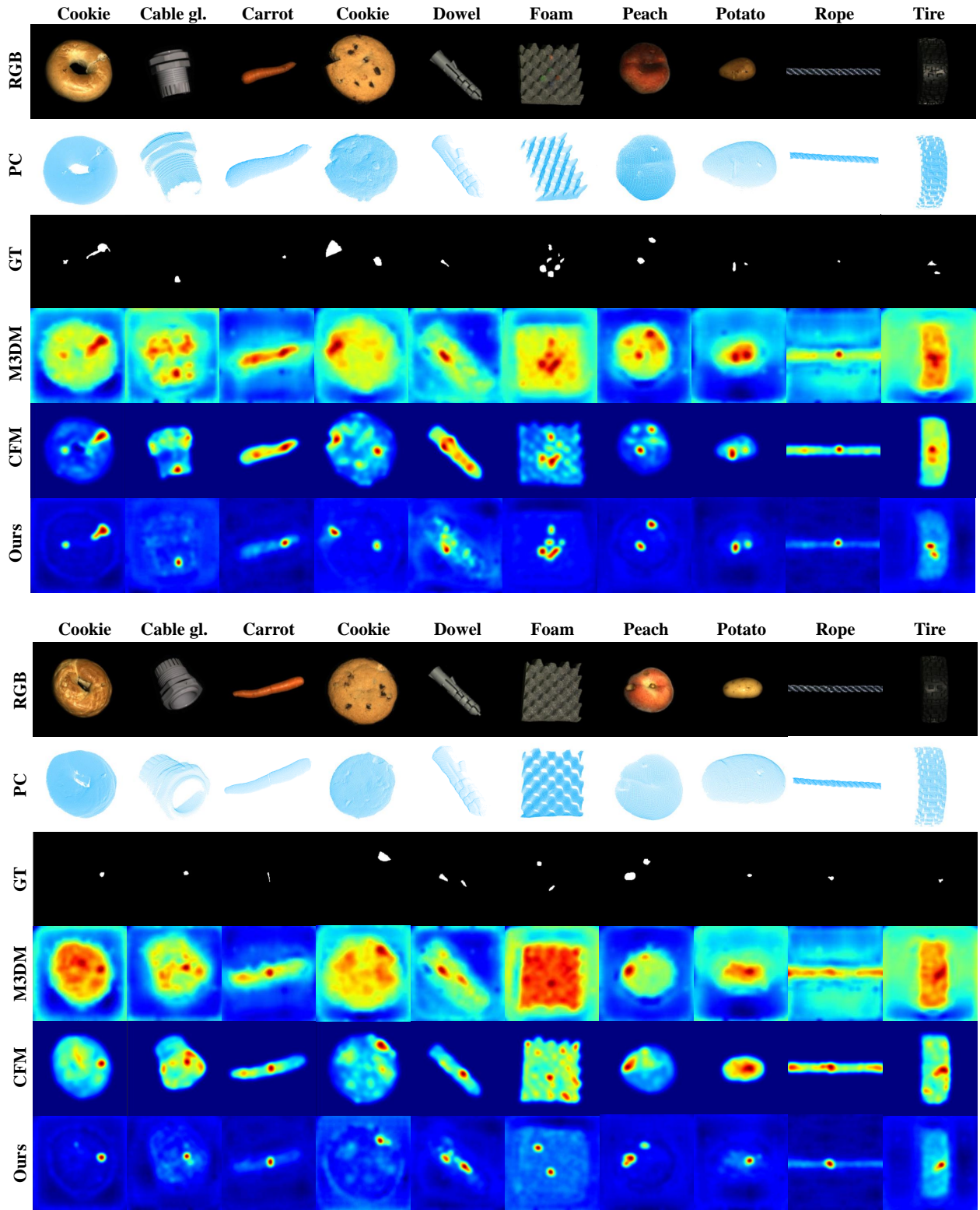


Fig. 4. Additional qualitative results on MVTEC-3D AD.